






A Sliding-Mode Control in a New Reference Frame for Three-Phase UPFR With Extended Control Range

Jose-Pascual Chico-Villegas , *Student Member, IEEE*, Ramon Guzman , *Senior Member, IEEE*, Luis Garcia de Vicuña , Miguel Castilla , and Àngel Borrell 

Abstract—This article presents a new switching strategy for a unity power factor rectifier (UPFR) using sliding-mode control (SMC). The traditional SMC in the natural frame suffers from a cross-coupling problem among controllers due to the neutral point voltage. To address this issue, a nonlinear transformation is applied to obtain the voltages and currents in a new 2-D reference frame. Based on the transformed variables, a nonlinear model is derived, and two different sliding-mode surfaces are designed using hysteresis band comparators. The nonlinear transformation is based on a switching strategy that not only avoids the cross-coupling problem but also injects a third harmonic in the control signal, providing an extended control range. As a result, a SMC is designed, providing relevant properties such as output voltage robustness, fast transient response against sudden load changes, and grid-voltage sags. Experimental results are provided to validate the theoretical contributions of this article.

Index Terms—Nonlinear control, sliding-mode control (SMC), third-harmonic injection, unity power factor rectifier (UPFR).

I. INTRODUCTION

THE unity power factor rectifiers (UPFRs) are widely employed as active front-end converters. Usually, the ac to dc conversion is done using a diode full-bridge rectifier which is the simplest solution, but it provides a low power factor and grid harmonics.

Manuscript received 6 October 2023; revised 24 January 2024 and 20 March 2024; accepted 22 April 2024. This work was supported in part by I+D+i PID2021-122835OB-C21 research project through MCIN/AEI/10.13039/501100011033 and FEDER “Una manera de hacer Europa.” (Corresponding author: Jose-Pascual Chico-Villegas.)

Jose-Pascual Chico-Villegas, Luis Garcia de Vicuña, and Miguel Castilla are with the Electronic Engineering Department, Technical University of Catalonia, 08800 Vilanova i la Geltrú, Spain (e-mail: jose.pascual.chico; jose.luis.garcia.de.vicuna; miguel.castilla@upc.edu).

Ramon Guzman is with the Automatic Control Department, Technical University of Catalonia, 08028 Barcelona, Spain (e-mail: ramon.guzman@upc.edu).

Àngel Borrell is with the Department of Electrical Engineering, Escola Universitària Salesiana de Sarrià, 08017 Barcelona, Spain (e-mail: aborrell@euss.es).

Color versions of one or more figures in this article are available at <https://doi.org/10.1109/TIE.2024.3395795>.

Digital Object Identifier 10.1109/TIE.2024.3395795

The control of UPFR has been addressed using various methods such as model predictive control (MPC) [1], [2], [3], fuzzy control [4], [5], neural networks [6], and one-cycle control [7]. However, limited research has been conducted on SMC using hysteresis comparators [8], [9]. The approaches of SMC with hysteresis comparators are based on forcing the sliding surface within a hysteresis band [10], [11], [12]. Besides, the solutions based on hysteresis comparators usually are designed in the natural reference frame using one controller for each phase-leg resulting in sliding losses and a variable switching frequency due to the interference among controllers [13]. Moreover, the conventional SMC with hysteresis comparators makes it difficult to extend the control range, contrary to the conventional modulation methods such as PWM and space-vector modulation [14], which allows to extend the control range and to reduce the capacitor voltage value [15].

Some solutions were proposed in the literature to solve the interference between controllers and to fix the switching frequency. In [16] and [17], a feed-forward calculation of the hysteresis bands is adopted to reduce the interference among controllers. In [18], a linear transformation is used to decouple the controllers, but this implementation depends on the converter parameters. In [19], the authors propose variable-band hysteresis using analog current controllers to achieve a similar harmonic performance as a space-vector modulation. The greatest difficulty of implementing these controllers is the cancelation of high-frequency control signals. To avoid these problems, some sliding-mode control (SMC) solutions can be found in the literature. In [20] and [21], an SMC with a Kalman filter is used to remove the interference among controllers with the advantage that the proposed decoupling method is practically independent of the system parameters. However, the implementation of this algorithm requires a high computational burden. Based on a vector operation technique, an alternative approach is presented in [22]. This approach solves the coupling problem using a switching scheme that has the advantage of reducing the commutation losses but reduces the control range.

It is well known that the control range can be augmented by injecting a third harmonic in the PWM signals or using a space-vector modulator [23], [24], [25], [26], [27], [28], [29]. This technique is an open topic in hysteresis controller design. In [19] and [30], a third harmonic is added in the hysteresis

TABLE I
COMPARISON

	[19]	[20]	[21]	[22]	proposed
Control Approach	Dead-Time Compensation and Variable Hysteresis Bands	Kalman Estimator and SMC	PI with feed-forward, SMC, Variable Hysteresis Bands, and Switching Decision Algorithm	PI, SMC, and Variable Hysteresis Bands	PI with feed-forward, SMC, Variable Hysteresis Bands, and Switching Decision Algorithm
Implementation	Analog and Digital	Digital	Digital	Digital	Digital
Implementation Complexity	High	High	Low	Medium	Low
Computation Burden	Low	High	Low	Low	Low
Load Variation	Yes	Yes	Yes	Yes	Yes
Voltage sags	No	No	Yes	No	Yes
Control Range	Extended	Extended	Reduced	Reduced	Extended

controllers to obtain a wider control range. In [20], a switching surface that includes the neutral point voltage is defined to impose a third harmonic in the control signals.

Table I compares the proposed method with previous approaches to solving the cross-coupling and control range limits. Some of these solutions, such as the analog design of the controller in [19] and the use of a Kalman filter in [20] result in higher complexity implementations. Also, the Kalman filter in [20] increases the computation burden considerably. In [21] and [22], similar approaches are proposed. Both use a feed-forward term to ensure a good dynamic response but only [21] is designed to be robust during voltage sags. Concerning the control range, Holmes et al. [19] and Guzman et al. [20] offer the same control range extension as the proposed method but at the cost of higher implementation complexity and a high computation burden, respectively. In [21], the control range is not extended. In [22], the commutation losses are reduced at the cost of limiting the control range. All the comparison methods are robust against load changes but only [21] and the proposed method are robust against grid-voltage sags. Regarding the proposed method, it can be implemented using a low computation burden providing a good dynamic response and excellent robustness against load variations and grid-voltage sags and an extended control range.

This work contributes not only to the control of UPFR converters but also proposes a new switching strategy that overcomes the aforementioned limitations. To this end, a nonlinear transformation and a UPFR model are derived in a bidimensional reference frame. This approach allows for designing free-interference controllers, addressing the limitations associated with traditional SMC using hysteresis comparators.

This article is organized as follows. Section II shows the three-phase UPFR model. Section III presents conventional SMC. Section IV shows the proposed switching strategy. Section V gives the experimental results of the designed control algorithm. Section VI concludes the article.

II. THREE-PHASE UPFR MODEL

The circuit diagram of a three-phase UPFR is presented in Fig. 1. The analysis of this circuit leads to the following differential equations:

$$L \frac{di_a}{dt} = v_a - \frac{v_0}{2} u_a + v_n \quad (1)$$

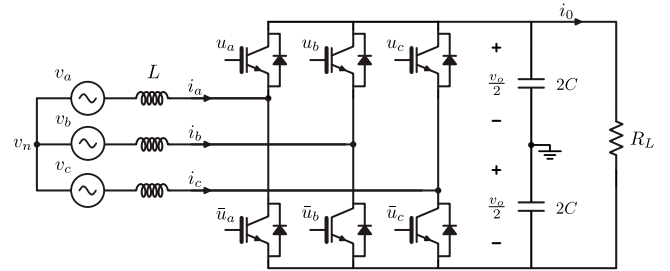


Fig. 1. Circuit diagram of a three-phase UPFR.

$$L \frac{di_b}{dt} = v_b - \frac{v_0}{2} u_b + v_n \quad (2)$$

$$L \frac{di_c}{dt} = v_c - \frac{v_0}{2} u_c + v_n \quad (3)$$

$$C \frac{dv_o}{dt} = \frac{u_a}{2} i_a + \frac{u_b}{2} i_b + \frac{u_c}{2} i_c - i_o \quad (4)$$

where v_n is the neutral voltage expressed as

$$v_n = \frac{v_0}{6} (u_a + u_b + u_c) \quad (5)$$

being u_a , u_b , and $u_c \in \{-1, 1\}$, v_a , v_b , and v_c are the natural components of the grid voltages, i_a , i_b , and i_c are the abc components of the grid current, i_o and v_o are the output current and output voltage, and L and C are the inductance and capacitor values, respectively.

III. CONVENTIONAL SMC

To ensure a unity power factor, the switching surfaces should be defined as

$$S_i = i_i - i_i^* \quad (6)$$

$$i_i^* = k v_i \quad (7)$$

where the subscript $i = [a, b, c]$ indicates the phase-leg and k is a control gain, conventionally implemented by a PI controller. Using (1)–(7), the sliding dynamics can be represented by

$$\dot{S}_i = \frac{1}{L} \left(v_i - \frac{v_o}{2} u_i + \frac{v_o}{6} (u_a + u_b + u_c) \right) - \frac{d(kv_i)}{dt}. \quad (8)$$

The cross-coupling problem is evidenced by the sliding-mode dynamics equation (8), where each phase-leg (a , b , and c) is affected by all the three control signals (u_a , u_b , and u_c). This issue will be addressed in Section IV-B.

To study the control range of the conventional SMC, it is necessary to analyze the equivalent control expressions. These expressions play a similar role to the duty cycle in PWM converters and can be derived from the invariance conditions $S = 0$ and $\dot{S} = 0$ [31]. Applying these conditions to (8), and considering $u_{eqa} + u_{eqb} + u_{eqc} = 0$, leads to

$$u_{eqi} = \frac{2}{v_o} \left(v_i - L \frac{d(kv_i)}{dt} \right). \quad (9)$$

These equivalent control signals are a function of the grid voltages defined as

$$v_a = V_p \sin(\omega t) \quad (10)$$

$$v_b = V_p \sin(\omega t - 2\pi/3) \quad (11)$$

$$v_c = V_p \sin(\omega t - 4\pi/3) \quad (12)$$

where V_p is the grid-voltage peak value and ω is the grid frequency. Then, using (10)–(12) in (9)

$$u_{eqa} = 2A \sin(\omega t - \theta) \quad (13)$$

$$u_{eqb} = 2A \sin\left(\omega t - \frac{2\pi}{3} - \theta\right) \quad (14)$$

$$u_{eqc} = 2A \sin\left(\omega t - \frac{4\pi}{3} - \theta\right) \quad (15)$$

where

$$A = \frac{V_p}{v_o} \sqrt{1 + (Lk\omega)^2} \quad (16)$$

$$\theta = \tan^{-1}(Lk\omega) \quad (17)$$

being V_p the peak grid voltage and θ the phase shift. Taking into account that the equivalent controls are limited by the minimum and maximum values of the control variables (13)–(16), that is, $-1 < u_{eqi} < 1$, the output voltage must accomplish the following inequality to avoid the saturation of the controller:

$$v_o > 2V_p \sqrt{1 + (Lk\omega)^2}. \quad (18)$$

This expression shows the minimum output voltage to avoid the controller saturation for the conventional SMC. Besides, the phase shift (17) is relevant to the proposed switching strategy to extend the control range and its influence on the proposed control will be detailed in Section IV-G.

IV. PROPOSED SWITCHING STRATEGY

To avoid the drawbacks previously mentioned, the proposed SMC uses only two switching surfaces avoiding interferences between controllers. Through a suitable selection of the converter switching scheme, it is possible to include a third harmonic in the equivalent controls.

Fig. 2 shows the proposed sliding-mode controller block diagram. Previously, the first harmonics of the grid voltages are measured to generate the inductor current references. Then, the controller is implemented in a new reference frame, named 1–2 reference frame. The first block implements a nonlinear transformation to obtain inductor currents, and grid voltages in 1–2 reference frame, from input currents and voltages in the

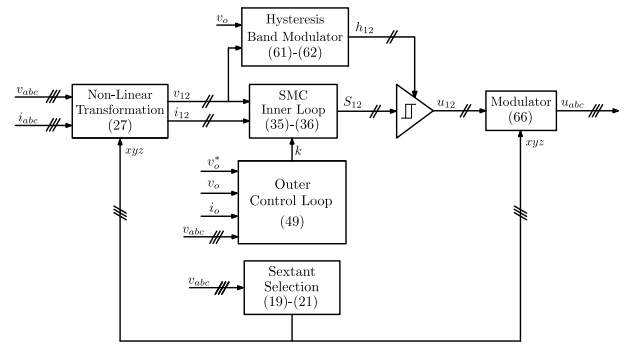


Fig. 2. Proposed SMC scheme in 1–2 reference frame.

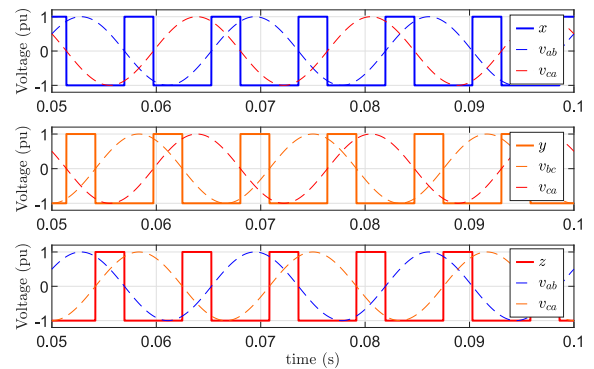


Fig. 3. Functions xyz and phase-to-phase voltages.

natural frame. In the second block, the switching surfaces S_1 and S_2 are implemented in conjunction with variable hysteresis band modulators to obtain fixed switching frequency and to determine the control signals u_1 and u_2 . Besides, the input current amplitude control k is implemented in the outer control loop block to achieve robustness in the output voltage against load step changes and grid-voltage sags. Finally, a modulator generates the control signals u_a , u_b , and u_c in the natural reference frame.

The switching control technique is based on dividing the line cycle in sextants according to the sign of the following variables named x , y and z which are defined as:

$$x = \text{sgn}(v_{ab}v_{ca}) \quad (19)$$

$$y = \text{sgn}(v_{bc}v_{ca}) \quad (20)$$

$$z = \text{sgn}(v_{ab}v_{bc}) \quad (21)$$

where sgn denotes the sign function and v_{ab} , v_{bc} , and v_{ca} are the phase-to-phase grid voltages expressed as follows:

$$v_{ab} = \sqrt{3}V_p \sin(\omega t + \pi/6) \quad (22)$$

$$v_{bc} = \sqrt{3}V_p \sin(\omega t - \pi/2) \quad (23)$$

$$v_{ca} = \sqrt{3}V_p \sin(\omega t + 5\pi/6). \quad (24)$$

The functions x , y , and z are represented in Fig. 3. The sign of these functions determines which one of the three possible switching schemes is used. Besides, to control the states of the converter switches, two new control variables u_1 and u_2 are

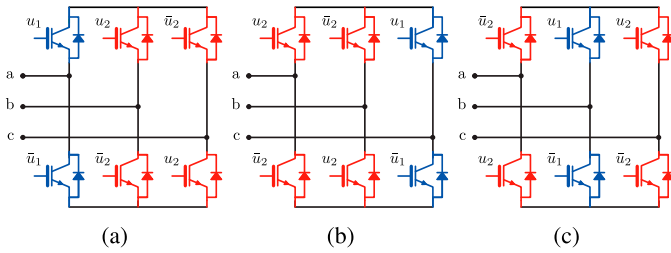


Fig. 4. Switching schemes and control actions for (a) $x = 1$, (b) $y = 1$, and (c) $z = 1$, according to Table II.

used. The value of these control variables determines the state of the switches. When a control variable is 1, the corresponding switch is in ON state and when is -1 the switch is in OFF state. Fig. 4 shows these switching schemes where the new control variables are depicted. As can be seen in Fig. 4, the switches of one phase-leg are controlled by using u_1 and \bar{u}_1 , and the remaining phase-legs are controlled by bipolar switching using the control variables u_2 and \bar{u}_2 , being $\bar{u}_1 = -\text{sgn}(u_1)$ and $\bar{u}_2 = -\text{sgn}(u_2)$. In Table II, each switching scheme is selected following the next procedure.

- 1) When $x = 1$, the phase-legs b and c are controlled by u_2 using a bipolar switching scheme and the phase-leg a is controlled by u_1 .
- 2) When $y = 1$, the phase-legs a and b are controlled by u_2 using a bipolar switching scheme and the phase-leg c is controlled by u_1 .
- 3) When $z = 1$, the phase-legs a and c are controlled by u_2 using a bipolar switching scheme and the phase-leg b is controlled by u_1 .

A. Nonlinear Transformation

Table II shows for each x, y, z combination the non-linear functions f_1 and f_2 . Each function can represent currents or voltages in 1–2 reference frame. In this table, the function f_1 is related to the independently controlled phase-leg and, f_2 is related to the phase-legs that use the bipolar switching scheme. According to Table II, these functions can be expressed as

$$f_1 = \frac{x+1}{2}f_a + \frac{y+1}{2}f_b + \frac{z+1}{2}f_c \quad (25)$$

$$f_2 = \frac{x+1}{2}(f_b - f_c) + \frac{y+1}{2}(f_a - f_b) + \frac{z+1}{2}(f_c - f_a) \quad (26)$$

where f_a, f_b , and f_c represent currents or voltages indistinctly. Taking into account that $f_a + f_b + f_c = 0$, the transformation can be expressed as

$$\begin{bmatrix} f_1 \\ f_2 \end{bmatrix} = \frac{1}{2} \begin{bmatrix} x-y & z-y \\ 2(y-z) & x-z \end{bmatrix} \begin{bmatrix} f_a \\ f_b \end{bmatrix}. \quad (27)$$

Fig. 5 shows the voltages v_1 and v_2 in the new reference frame using (27). As it can be seen, the sign functions provoke discontinuities in these voltages each 60° .

B. UPFR Model in 1–2 Reference Frame

When the proposed switching control strategy is applied to a three-phase UPFR, three different switching schemes are derived. The dynamic equations in the natural frame for the first switching scheme shown in Fig. 4(a) can be obtained from (1)–(5), Table II and considering that $u_c = -u_b$

$$L \frac{di_a}{dt} = v_a - \frac{v_o}{2}u_a + v_n \quad (28)$$

$$L \frac{di_b}{dt} = v_b - \frac{v_o}{2}u_b + v_n \quad (29)$$

$$L \frac{di_c}{dt} = v_c + \frac{v_o}{2}u_b + v_n \quad (30)$$

$$C \frac{dv_o}{dt} = \frac{u_a}{2}i_a + \frac{u_b}{2}(i_b - i_c) - i_o. \quad (31)$$

From the previous equations, it is accomplished that $v_n = (v_o/6)u_a$.

Subtracting (30) from (29) and identifying from Table II that $v_1 = v_a, v_2 = v_b - v_c, i_1 = i_a, i_2 = i_b - i_c, u_1 = u_a$, and $u_2 = u_b = -u_c$, leads to

$$L \frac{di_1}{dt} = v_1 - \frac{v_o}{3}u_1 \quad (32)$$

$$L \frac{di_2}{dt} = v_2 - v_o u_2 \quad (33)$$

$$C \frac{dv_o}{dt} = \frac{u_1}{2}i_1 + \frac{u_2}{2}i_2 - i_o. \quad (34)$$

The previous equations constitute the three-phase UPFR model in 1–2 reference frame since identical results are obtained for the remaining switching schemes. Note that in this model, the inductor currents differential equations only depend on its own control variable. This model provides a proper mathematical description of the converter and will be used to design a SMC in this reference frame without interference between controllers. This solution will allow fixing the switching frequency by using variable-band hysteresis modulators.

C. Controller Design

Two different control loops are used for controlling a UPFR. The inner control is responsible for tracking the first harmonic of the grid voltages assuring a unity power factor. The outer control loop has as main objective to regulate the output voltage.

1) *Inner Control Loop*: To achieve sinusoidal input currents in phase with the grid voltages, the following sliding surfaces are proposed:

$$S_1 = i_1 - i_1^* \quad (35)$$

$$S_2 = i_2 - i_2^* \quad (36)$$

where i_1 and i_2 are the input currents and i_1^* and i_2^* are the reference currents defined as

$$i_1^* = kv_1 \quad (37)$$

$$i_2^* = kv_2 \quad (38)$$

being v_1 and v_2 are the grid voltages in 1–2 reference frame and k is the input current amplitude.

2) *Outer Control Loop*: This controller is designed to regulate the output voltage ensuring a fast dynamic behavior that

TABLE II
SWITCHING SCHEMES, NONLINEAR FUNCTIONS, AND CONTROL ACTIONS ACCORDING TO THE SIGN OF x , y , AND z

Sign			Switching Scheme			Nonlinear Transformation		Control Actions		
x	y	z	Independent Switching	Bipolar Switching		f_1	f_2	u_a	u_b	u_c
1	-1	-1	a	b	c	f_a	$f_b - f_c$	u_1	u_2	\bar{u}_2
-1	1	-1	c	a	b	f_c	$f_a - f_b$	u_2	\bar{u}_2	u_1
-1	-1	1	b	c	a	f_b	$f_c - f_a$	\bar{u}_2	u_1	u_2

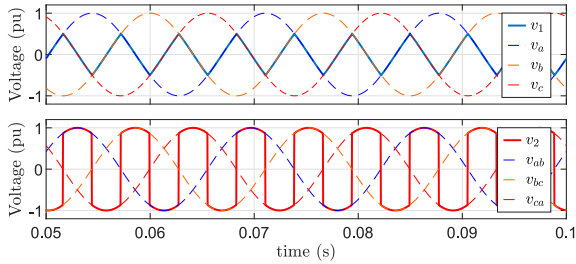


Fig. 5. Voltages in 1-2 reference frame.

avoids the distortion of the input currents. The fast dynamic response under load step changes and disturbances can be met by introducing a feed-forward term in the controller. To this end, the equivalent control expressions should be derived using (32)–(38)

$$u_{eq1} = \frac{3}{v_o} \left(v_1 - L \frac{d(kv_1)}{dt} \right) \quad (39)$$

$$u_{eq2} = \frac{1}{v_o} \left(v_2 - L \frac{d(kv_2)}{dt} \right). \quad (40)$$

Then, the output voltage dynamics can be obtained using (39)–(40) in (34), which leads to

$$C \frac{dv_o}{dt} = \frac{k}{v_o} \left(1 - L \frac{dk}{dt} \right) \left(\frac{3v_1^2 + v_2^2}{2} \right) - \frac{Lk^2}{v_o} \frac{d}{dt} \left(\frac{3v_1^2 + v_2^2}{2} \right) - i_o. \quad (41)$$

For a general case, the grid voltages in the natural frame can be expressed by their positive and negative sequence as

$$v_a = V^+ \sin(\omega t) + V^- \sin(\omega t + \phi) \quad (42)$$

$$v_b = V^+ \sin(\omega t - 2\pi/3) + V^- \sin(\omega t + 2\pi/3 + \phi) \quad (43)$$

$$v_c = V^+ \sin(\omega t - 4\pi/3) + V^- \sin(\omega t + 4\pi/3 + \phi) \quad (44)$$

where ϕ is the phase angle of the negative sequence relative to the positive sequence and the parameters V^+ and V^- are the positive and negative grid-voltage amplitudes, respectively. Now, considering (42)–(44) and Table II

$$\begin{aligned} \frac{3v_1^2 + v_2^2}{2} &= (v_a^2 + v_b^2 + v_c^2) \\ &= \frac{3}{2} \left(V^{+2} + V^{-2} - 2V^+V^- \cos(2\omega t + \phi) \right). \end{aligned} \quad (45)$$

Substituting (45) in (41) leads to

$$\begin{aligned} C \frac{dv_o}{dt} &= \frac{3k}{2v_o} \left(1 - L \frac{dk}{dt} \right) (V^{+2} + V^{-2} \\ &\quad - 2V^+V^- \cos(2\omega t + \phi)) \\ &\quad - \frac{3Lk^2}{2v_o} (4\omega V^+V^- \sin(2\omega t + \phi)) - i_o. \end{aligned} \quad (46)$$

Notice that (46) depends on the derivative of k . The dynamics of v_o can be rewritten by considering $1 \gg L(dk/dt)$ which is a widely accepted approximation [32], yielding

$$\begin{aligned} C \frac{dv_o}{dt} &= \frac{3k}{2v_o} \left(V^{+2} + V^{-2} - 2V^+V^- \cos(2\omega t + \phi) \right) \\ &\quad - \frac{3Lk^2}{2v_o} (4\omega V^+V^- \sin(2\omega t + \phi)) - i_o. \end{aligned} \quad (47)$$

Averaging the previous equation, it leads to

$$C \frac{d\langle v_o \rangle}{dt} \simeq \frac{3k}{2\langle v_o \rangle} \left(V^{+2} + V^{-2} \right) - \langle i_o \rangle \quad (48)$$

where $\langle v_o \rangle$ is the average value of the output voltage. This equation allows to conceive an input current amplitude control k , which linearizes the average output voltage dynamics under asymmetrical faults and load step changes. The proposed control gain k is given by

$$\begin{aligned} k &= \frac{2\langle v_o \rangle}{3(V^{+2} + V^{-2})} ((k_p(v_o^* - \langle v_o \rangle)) \\ &\quad + k_i \int (v_o^* - \langle v_o \rangle) dt + \langle i_o \rangle) \end{aligned} \quad (49)$$

where k_p and k_i are the control gains and i_o is a feed-forward term of the output current. The positive and negative sequence amplitudes are obtained using a sequence detector [33], [34]. Substituting (49) in (48) leads to

$$C \frac{d\langle v_o \rangle}{dt} \simeq k_p(v_o^* - \langle v_o \rangle) + k_i \int (v_o^* - \langle v_o \rangle) dt. \quad (50)$$

Then, the closed-loop dynamics equation can be found

$$\frac{d^2\langle v_o \rangle}{dt^2} + \frac{k_p}{C} \frac{d\langle v_o \rangle}{dt} + \frac{k_i}{C} \langle v_o \rangle = \frac{k_i}{C} v_o^*. \quad (51)$$

The control gain k linearizes the v_o dynamics and guarantees stable dynamics if k_p and k_i are positive values. This controller provides a high output voltage robustness against load changes and grid-voltage sags.

D. Control Law

In the sliding control, the sliding mode reaching conditions guarantee the existence of the sliding regime [35]. These conditions are often given by

$$S_j \dot{S}_j < 0 \quad (52)$$

where $j = 1, 2$. The first derivative of the surfaces can be obtained using (32)–(36) and can be expressed as

$$\dot{S}_1 = \frac{1}{L} \left(v_1 - \frac{v_o}{3} u_1 \right) - \frac{d(kv_1)}{dt} \quad (53)$$

$$\dot{S}_2 = \frac{1}{L} \left(v_2 - v_o u_2 \right) - \frac{d(kv_2)}{dt} \quad (54)$$

where the control variable u_1 can be defined as

$$u_1 = \begin{cases} u_1^+, & \text{if } S_1 > 0 \\ u_1^-, & \text{if } S_1 < 0 \end{cases} \quad (55)$$

being $u_1 \in \{-1, 1\}$.

Applying (55) to the reaching condition (52), the control law can be determined as follows.

If $S_1 > 0$, then $\dot{S}_1 < 0$ and $u_1 = u_1^+$

$$\dot{S}_1 = \frac{1}{L} \left(v_1 - \frac{v_o}{3} u_1^+ \right) - \frac{d(kv_1)}{dt} < 0. \quad (56)$$

If $S_1 < 0$, then $\dot{S}_1 > 0$ and $u_1 = u_1^-$

$$\dot{S}_1 = \frac{1}{L} \left(v_1 - \frac{v_o}{3} u_1^- \right) - \frac{d(kv_1)}{dt} > 0. \quad (57)$$

From (56) and (57), one has the following:

$$\frac{v_o}{3L} (u_1^- - u_1^+) < 0. \quad (58)$$

From this expression, the control law for the switching surface S_1 can be expressed as

$$u_1 = \begin{cases} u_1^+ = 1, & \text{if } S_1 > 0 \\ u_1^- = -1, & \text{if } S_1 < 0. \end{cases} \quad (59)$$

Following similar steps for the switching surface S_2 :

$$u_2 = \begin{cases} u_2^+ = 1, & \text{if } S_2 > 0 \\ u_2^- = -1, & \text{if } S_2 < 0. \end{cases} \quad (60)$$

E. Variable Hysteresis Band Modulator

To obtain a practically fixed switching frequency, a hysteresis band generator was implemented together with a switching decision algorithm. The expressions of the hysteresis bands using hysteresis comparators are obtained using a similar procedure to that proposed in [19], [21], obtaining

$$h_1 = \frac{v_o}{12L f_{sw}} \left(1 - \left(\frac{3v_1}{v_o} \right)^2 \right) \quad (61)$$

$$h_2 = \frac{v_o}{4L f_{sw}} \left(1 - \left(\frac{v_2}{v_o} \right)^2 \right) \quad (62)$$

where f_{sw} is the switching frequency, and h_1 and h_2 are the width of the hysteresis bands.

F. Modulator

To determine the state of the switches, it is necessary to obtain u_a , u_b , and u_c through a transformation applied to the control variables u_1 and u_2 . Table II represents the relationship between the control variables in the natural frame and the 1–2 reference frame according to x , y , and z . Following Table II, the control variables in abc frame are given by

$$u_a = \frac{x+1}{2} u_1 + \frac{y+1}{2} u_2 + \frac{z+1}{2} \bar{u}_2 \quad (63)$$

$$u_b = \frac{x+1}{2} u_2 + \frac{y+1}{2} \bar{u}_2 + \frac{z+1}{2} u_1 \quad (64)$$

$$u_c = \frac{x+1}{2} \bar{u}_2 + \frac{y+1}{2} u_1 + \frac{z+1}{2} u_2. \quad (65)$$

The previous expressions constitute the modulator equations and can be represented in matrix form as

$$\begin{bmatrix} u_a \\ u_b \\ u_c \end{bmatrix} = \frac{1}{2} \begin{bmatrix} x+1 & y-1 \\ z+1 & x-y \\ y+1 & z-x \end{bmatrix} \begin{bmatrix} u_1 \\ u_2 \end{bmatrix}. \quad (66)$$

G. Equivalent Controls and Third-Harmonic Injection

This section is dedicated to show that the proposed SMC produces the same effect of a third-harmonic injection of the grid frequency in their equivalent controls. To evaluate the equivalent controls in abc reference frame is necessary to analyze in detail the modulators performance during a grid period. Every equivalent control signal in the natural frame adopts three different expressions in half grid period, one for each possible switching scheme ($x = 1$, $y = 1$, and $z = 1$). As an example, from Table II, and according to (39)–(40), the equivalent control signal for the phase-leg a can be derived as follows:

$$u_{eqa} |_{x=1} = u_{eq1} = \frac{3}{v_o} \left(v_a - L \frac{d(kv_a)}{dt} \right) = 3A \sin(\omega t - \theta) \quad (67)$$

$$u_{eqa} |_{y=1} = u_{eq2} = \frac{1}{v_o} \left(v_{ab} - L \frac{d(kv_{ab})}{dt} \right) = \sqrt{3}A \sin(\omega t - \theta + \pi/6) \quad (68)$$

$$u_{eqa} |_{z=1} = \bar{u}_{eq2} = \frac{1}{v_o} \left(-v_{ca} - L \frac{d(k(-v_{ca}))}{dt} \right) = -\sqrt{3}A \sin(\omega t - \theta + 5\pi/6) \quad (69)$$

where A and θ are defined in (16) and (17). Following a similar procedure, the equivalent controls for phase-legs b and c can be obtained. Table III shows the three equivalent control expressions for each control scheme and phase-leg.

Fig. 6(a) depicts x , y , z and u_{eqa} considering $\theta = 0$. As shown in this figure, the switching control technique extends the control range since it produces a similar effect of introducing a third harmonic in the control signals. Fig. 6(b) shows u_{eqa} with $\theta = 20.65^\circ$. In this case, u_{eqa} is distorted due to $\theta \neq 0$. To obtain the waveform without distortion, the functions x , y , and z will be delayed θ in the implementation.

To calculate the control range extension, it is necessary to obtain the maximum values for the equivalent control signals

TABLE III
EQUIVALENT CONTROL ACTIONS IN abc BY CONTROL SCHEMES

x	y	z	u_{eqa}	u_{eqb}	u_{eqc}
1	-1	-1	$3A \sin(\omega t - \theta)$	$-\sqrt{3}A \sin(\omega t - \theta + \pi/2)$	$\sqrt{3}A \sin(\omega t - \theta + \pi/2)$
-1	1	-1	$\sqrt{3}A \sin(\omega t - \theta + \pi/6)$	$-\sqrt{3}A \sin(\omega t - \theta + \pi/6)$	$3A \sin(\omega t - \theta - 4\pi/3)$
-1	-1	1	$-\sqrt{3}A \sin(\omega t - \theta + 5\pi/6)$	$3A \sin(\omega t - \theta - 2\pi/3)$	$\sqrt{3}A \sin(\omega t - \theta + \pi/2)$

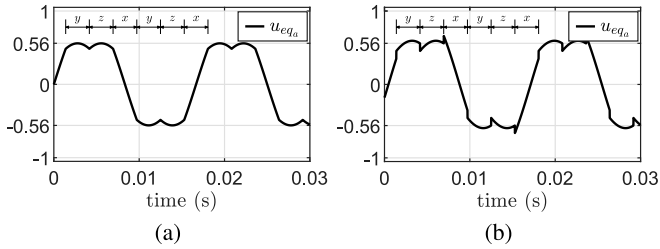


Fig. 6. Equivalent control signal u_{eqa} with (a) $\theta = 0^\circ$ and with (b) $\theta = 20.65^\circ$ considering $L = 5$ mH, $k = 0.2$ and $\omega = 2\pi 60$ rad/s.

using the conventional SMC and the proposed method. It can be deduced from Table III that the maximum value for the equivalent controls are given by

$$u_{eqi_{\max}} |_{\text{proposed}} = \sqrt{3}A \quad (70)$$

where $i = a, b, c$. The maximum value for the conventional SMC equivalent controls can be deduced from (13)–(16)

$$u_{eqi_{\max}} |_{\text{conventional}} = 2A. \quad (71)$$

From the previous expressions, it can be seen that the proposed technique allows increasing the equivalent control maximum value to $2/\sqrt{3} \approx 1.15$ without saturating the controller, which represents an advantage against the conventional SMC.

V. EXPERIMENTAL RESULTS

This section presents the experimental tests implemented on a three-phase rectifier prototype built using a 2.3-kVA Guasch MTL-CBI0060F12IXHF full bridge as the power converter and a TMS320F28M36 floating-point DSP as the control platform. The grid voltages have been generated using a PACIFIC 360-AMX source. The system parameters are listed in Table IV. A photograph of the experimental setup is shown in Fig. 7.

A. Axis Decoupling

Fig. 8(a) shows the sliding switching surfaces S_a, S_b, S_c and their corresponding control signals $u_a, u_b,$ and u_c using a conventional SMC. As can be seen, the system is coupled since the change of the slopes on the sliding surfaces is not synchronized with their control actions. Equation (8) shows how the sliding dynamics for each phase-leg is influenced by the remaining control actions. In Fig. 8(a), each phase-leg control signal is not switching during a long period of time, leading to sliding losses. On the other hand, Fig. 8(b) shows the switching surfaces S_1 and S_2 , and the control actions u_1 and

TABLE IV
SYSTEM PARAMETERS

Symbol	Description	Value
L	Filter input inductance	5 mH
C	Output capacitor	1000 μF
v_o	DC-Link voltage	220 V
f_s	Sampling frequency	30 kHz
f_{sw}	Switching frequency	5 kHz
f_{grid}	Grid frequency	60 Hz
V_{grid}	Grid Voltage	50 V_{rms}
k_p	Proportional gain	0.002
k_i	Integral gain	1
R_L	Load	134 Ω

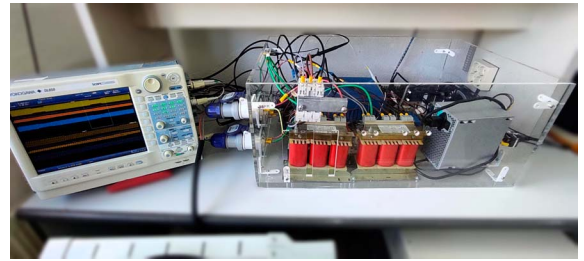


Fig. 7. Photograph of the experimental setup.

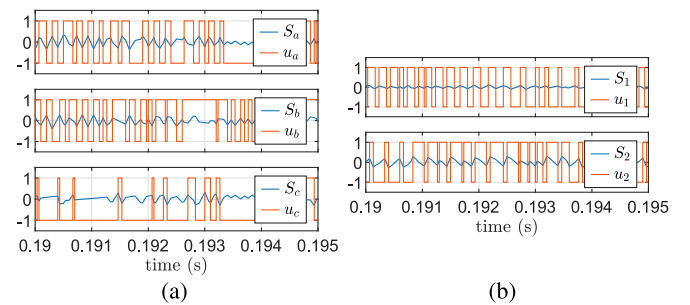


Fig. 8. Experimental results for sliding surfaces and control signals. (a) Conventional SMC. (b) Proposed SMC.

u_2 using the proposed control. In this case, the changes in the slopes of the switching surfaces coincide with the changes in the control signals, which proves that the system is decoupled avoiding sliding losses. The latter confirms that each sliding dynamic equation (53) and (54) only depends on its control actions u_1 and u_2 .

Fig. 9 depicts the switching surface S_1 and S_2 , (35)–(36), and their corresponding hysteresis bands h_1 and h_2 , (61)–(62),

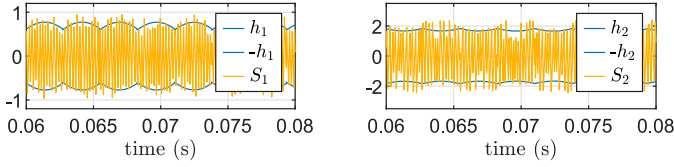


Fig. 9. Experimental results for sliding surfaces S_1 and S_2 and the variable hysteresis bands h_1 and h_2 .

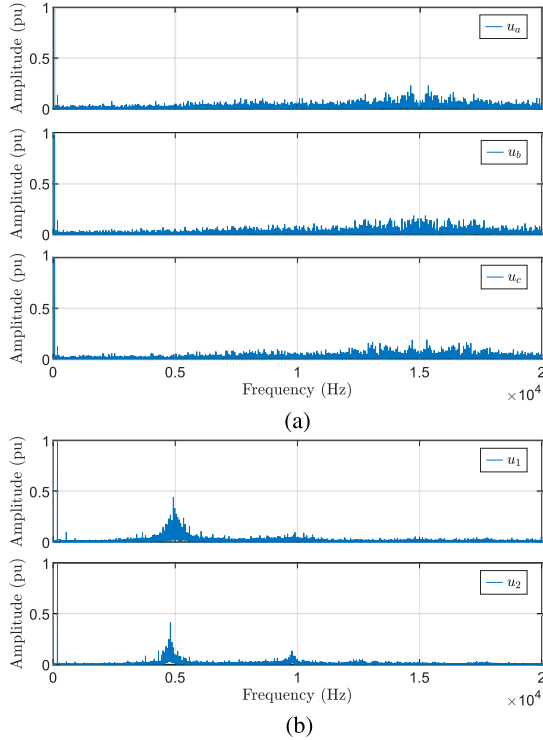


Fig. 10. Experimental spectrum for control signals. (a) Conventional SMC. (b) Proposed SMC.

respectively. It can be seen that the switching surfaces are practically inside their hysteresis bands.

Fig. 10 shows the experimental switching frequency spectrum using the conventional SMC and the proposed method. The conventional SMC suffers from variable switching frequency since no variable hysteresis bands can be used due to the interference among controllers. As a consequence, a spread switching frequency spectrum is obtained as shown in Fig. 10(a). Besides, with the proposed method, a variable band hysteresis modulator is used. Then, the switching frequency spectrum is concentrated around the desired switching frequency of 5 kHz as shown in Fig. 10(b).

B. Harmonic Distortion

Fig. 11 shows the harmonic spectrum of the grid current for the phase-leg a . The spectrum using the conventional SMC is shown in Fig. 11(a) and its THD is 1.077%. In contrast, when the proposed controller is employed, the THD is reduced to 0.489%. This proves the effectiveness of the proposed

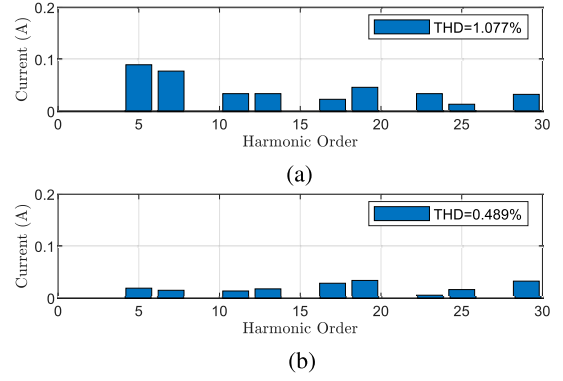


Fig. 11. Experimental THD of grid current i_a . (a) Conventional SMC. (b) Proposed SMC.

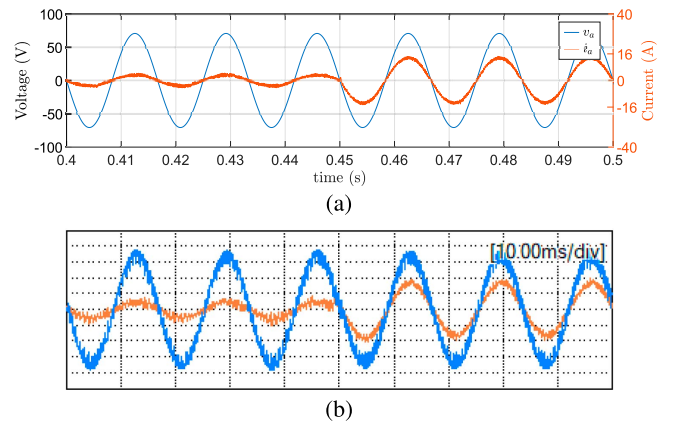


Fig. 12. Phase-a input voltage (20 V/div) and inductor current (8 A/div) in phase during a load step change from 372 to 1180 W. (a) Simulation result. (b) Experimental result.

method. Notice that the fundamental component is not represented to obtain a higher resolution in the rest of the harmonic components.

C. Dynamic Response

The proposed controller is tested during a load change from 372 to 1180 W. Fig. 12 shows the simulation and experimental results for the input voltage and current for the phase-leg a . In both cases, the dynamical response is similar, proving that the input current tracks the grid voltage, ensuring a unity power factor.

Fig. 13 shows the output voltage dynamic behavior and control amplitude k with and without feed-forward term during a load step change from 372 to 1180 W. In Fig. 13(a), the input current amplitude controller is based on a PI controller without a feed-forward term. In this figure, the amplitude control of the input current gain k evolves smoothly, producing a significant drop in the output voltage as can be seen in Fig. 13(a). The same experiment is performed in Fig. 13(b). In this case, a load current feed-forward control is used (49). In Fig. 13(b), the transient response of the gain k is almost instantaneous and

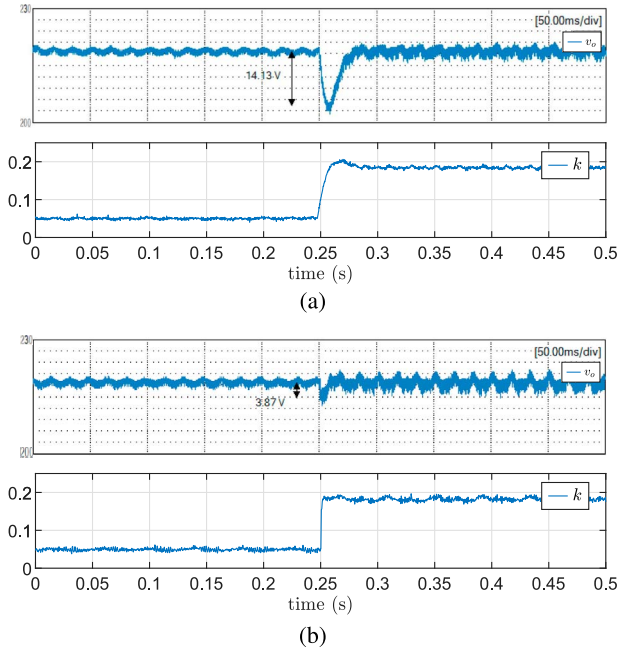


Fig. 13. Experimental result for output voltage (3V/div) and gain k during a load step change from 372 to 1180 W (a) without feed-forward term and (b) with feed-forward term.

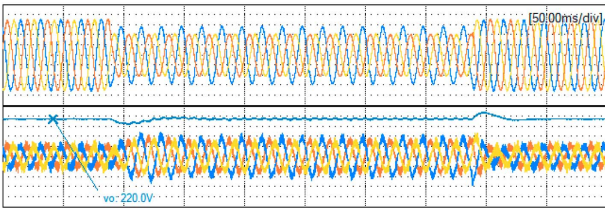


Fig. 14. Experimental results during an asymmetrical fault ($V^+ = 0.65V_p$ and $V^- = 0.12V_p$): (Top) grid voltages (50 V/div), and (bottom) grid currents (5A/div) and output voltage (30 V/div).

the output voltage is practically not affected by the load change as shown in Fig. 13(b).

The proposed controller has been tested under a grid-voltage sag. This sag is characterized by the positive and negative sequence of the grid voltages being $V^+ = 0.65V_p$ and $V^- = 0.12V_p$ (42)–(44), with a phase angle $\phi = 0$. Fig. 14 shows the output voltage and the three-phase input current and voltage waveforms during the voltage sag. The figure shows that the inductor currents track the unbalanced grid voltages and the output voltage is practically not affected by the disturbance. It can be appreciated that the grid currents track the unbalanced grid voltages during the fault and the output voltage presents a ripple frequency component of $2\omega_o$, as expected.

D. Control Range Extension

The control signal u_a has been measured experimentally and its value can be 0 or 5 V. This signal is filtered to obtain its average value u_{eq_a} . Fig. 15(a) shows u_{eq_a} for a conventional SMC. Fig. 15(b) depicts u_{eq_a} for the proposed control. As can

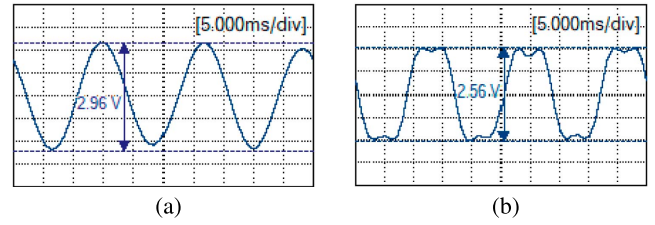


Fig. 15. Experimental result for u_{eq_a} (625mV/div) with (a) conventional SMC and (b) proposed control method.

be seen in Fig. 15, the amplitude of u_{eq_a} is reduced from 2.96 to 2.56 V with the proposed method increasing the equivalent control maximum value by a factor of 1.15 (70)–(71).

VI. CONCLUSION

In this article, an SMC control technique is proposed for three-phase UPFRs to solve the interference among controllers and extend the control range. Compared to other control schemes, this proposal has a better dynamic range and performance under sudden load changes and grid-voltage sags. In addition to this major contribution, the other results of this work have the following.

- 1) A new reference frame based on a nonlinear transformation which avoids interference among controllers.
- 2) The proposed SMC provides a unity power factor with high insensitivity of output voltage against sudden step load changes and grid-voltage sags.
- 3) Fixed switching frequency is obtained using variable hysteresis bands and a switching decision algorithm.
- 4) Experimental validation of the proposed control shows decoupling between controllers, a fast dynamic response and an extended control range.

Future work may explore the application of the proposed nonlinear transformation to other power converters.

REFERENCES

- [1] P. Cortés, J. Rodríguez, P. Antoniewicz, and M. Kazmierkowski, “Direct power control of an AFE using predictive control,” *IEEE Trans. Power Electron.*, vol. 23, no. 5, pp. 2516–2523, Sep. 2008.
- [2] S. Bayhan, “Grid voltage sensorless model predictive control for a single-phase T-type rectifier with an active power decoupling circuit,” *IEEE Access*, vol. 9, pp. 19161–19174, 2021.
- [3] Y. Sun, X. Feng, Z. Dai, and W. Ma, “A novel optimal voltage vector selection control strategy for Vienna rectifier,” *IEEE Access*, vol. 11, pp. 49422–49430, 2023.
- [4] H. Lin et al., “Fuzzy sliding-mode control for three-level NPC AFE rectifiers: A chattering alleviation approach,” *IEEE Trans. Power Electron.*, vol. 37, no. 10, pp. 11704–11715, Oct. 2022.
- [5] K. Y. Ahmed, N. Z. Bin Yahaya, V. S. Asirvadam, N. Saad, R. Kannan, and O. Ibrahim, “Development of power electronic distribution transformer based on adaptive PI controller,” *IEEE Access*, vol. 6, pp. 44970–44980, 2018.
- [6] A. S. Soliman, M. M. Amin, F. F. El-Sousy, and O. Mohammad, “Experimental validation for artificial data-driven tracking control for enhanced three-phase grid-connected boost rectifier in DC microgrids,” *IEEE Trans. Ind. Appl.*, vol. 59, no. 2, pp. 2563–2580, Mar./Apr. 2023.
- [7] Y. Tang, P. C. Loh, P. Wang, and F. H. Choo, “One-cycle-controlled three-phase PWM rectifiers with improved regulation under unbalanced and distorted input-voltage conditions,” *IEEE Trans. Power Electron.*, vol. 25, no. 11, pp. 2786–2796, Nov. 2010.

- [8] K. Rayane, M. Bougrine, H. Abu-Rub, A. Benalia, and M. Trabelsi, "Average model-based sliding mode control for quality improvement of a grid-connected PUC inverter," *IEEE J. Emerg. Sel. Topics Power Electron.*, vol. 11, no. 4, pp. 3765–3774, Aug. 2023.
- [9] A. I. Maswood and F. Liu, "A unity-power-factor converter using the synchronous-reference-frame-based hysteresis current control," *IEEE Trans. Ind. Appl.*, vol. 43, no. 2, pp. 593–599, Mar./Apr. 2007.
- [10] P. C. Loh, G. Bode, D. Holmes, and T. Lipo, "A time-based double-band hysteresis current regulation strategy for single-phase multilevel inverters," *IEEE Trans. Ind. Appl.*, vol. 39, no. 3, pp. 883–892, May/June 2003.
- [11] R. Davoodnezhad, D. G. Holmes, and B. P. McGrath, "A novel three-level hysteresis current regulation strategy for three-phase three-level inverters," *IEEE Trans. Power Electron.*, vol. 29, no. 11, pp. 6100–6109, Nov. 2014.
- [12] H. Komurcugil, S. Biricik, S. Bayhan, and Z. Zhang, "Sliding mode control: Overview of its applications in power converters," *IEEE Ind. Electron. Mag.*, vol. 15, no. 1, pp. 40–49, Mar. 2021.
- [13] N. Altin, S. Ozdemir, H. Komurcugil, and I. Sefa, "Sliding-mode control in natural frame with reduced number of sensors for three-phase grid-tied LCL-interfaced inverters," *IEEE Trans. Ind. Electron.*, vol. 66, no. 4, pp. 2903–2913, Apr. 2019.
- [14] A. Dey, P. P. Rajeevan, R. Ramchand, K. Mathew, and K. Gopakumar, "A space-vector-based hysteresis current controller for a general n-level inverter-fed drive with nearly constant switching frequency control," *IEEE Trans. Ind. Electron.*, vol. 60, no. 5, pp. 1989–1998, May 2013.
- [15] B. J. Pordanjani, A. Saleki, and M. T. Bina, "DSP-implementation of the SVM and THI-PWM techniques: Comparing THD and switching losses of cascaded H-bridge converter," in *Proc. 28th Iranian Conf. Elect. Eng. (ICEE)*, 2020, pp. 1–7.
- [16] W. Stefanutti and P. Mattavelli, "Fully digital hysteresis modulation with switching-time prediction," *IEEE Trans. Ind. Appl.*, vol. 42, no. 3, pp. 763–769, May/June 2006.
- [17] S. Buso, S. Fasolo, L. Malesani, and P. Mattavelli, "A dead-beat adaptive hysteresis current control," *IEEE Trans. Ind. Appl.*, vol. 36, no. 4, pp. 1174–1180, Jul./Aug. 2000.
- [18] W. Yan, J. Hu, V. Utkin, and L. Xu, "Sliding mode pulsewidth modulation," *IEEE Trans. Power Electron.*, vol. 23, no. 2, pp. 619–626, Mar. 2008.
- [19] D. G. Holmes, R. Davoodnezhad, and B. P. McGrath, "An improved three-phase variable-band hysteresis current regulator," *IEEE Trans. Power Electron.*, vol. 28, no. 1, pp. 441–450, Jan. 2013.
- [20] R. Guzman, L. G. de Vicuña, J. Morales, M. Castilla, and J. Miret, "Model-based active damping control for three-phase voltage source inverters with LCL filter," *IEEE Trans. Power Electron.*, vol. 32, no. 7, pp. 5637–5650, Jul. 2017.
- [21] R. Guzman, L. G. de Vicuña, J. Morales, M. Castilla, and J. Matas, "Sliding-mode control for a three-phase unity power factor rectifier operating at fixed switching frequency," *IEEE Trans. Power Electron.*, vol. 31, no. 1, pp. 758–769, Jan. 2016.
- [22] J. Morales, L. G. de Vicuña, R. Guzman, M. Castilla, and J. Miret, "Modeling and sliding mode control for three-phase active power filters using the vector operation technique," *IEEE Trans. Ind. Electron.*, vol. 65, no. 9, pp. 6828–6838, Sep. 2018.
- [23] H. Komurcugil and O. Kukrer, "Lyapunov-based control for three-phase PWM AC/DC voltage-source converters," *IEEE Trans. Power Electron.*, vol. 13, no. 5, pp. 801–813, Sep. 1998.
- [24] L. Han, Y. Zhang, X. Wang, and H. Yang, "Current harmonics minimization of model-free predictive current control for PWM rectifiers based on hybrid SVM," *IEEE J. Emerg. Sel. Topics Power Electron.*, vol. 12, no. 1, pp. 486–495, Feb. 2024.
- [25] Y. Ma, D. Jiang, Z. Liu, S. Yan, Z. Wang, and R. Qu, "Common-mode voltage elimination of dual three-phase motor with different angular displacements," *IEEE Trans. Ind. Electron.*, vol. 71, no. 6, pp. 5431–5442, Jun. 2024.
- [26] M. R. Arahal, M. J. Duran, F. Barrero, and S. Toral, "Analysis of variable third harmonic injection for five-phase IM," in *Proc. Eur. Control Conf. (ECC)*, Aug. 2009, pp. 4350–4355.
- [27] X. Ma, B. Li, G. Li, and Q. Zhu, "An SVPWM strategy with extended linear modulation range for dual three-phase machine drives under unbalanced power sharing conditions," *IEEE Trans. Power Electron.*, vol. 39, no. 4, pp. 4527–4541, Apr. 2024.
- [28] J. Huang and K. Li, "Eliminating common-mode voltage spikes in three-phase inverters through 12-section space-vector modulation," *IEEE Trans. Ind. Electron.*, vol. 71, no. 7, pp. 6471–6480, Jul. 2024.
- [29] H. Wang et al., "Fault-tolerant control for single-phase open-circuit and short-circuit fault in five-phase PMSM with third-order harmonic back EMF using coefficients reconfiguration," *IEEE Trans. Energy Convers.*, vol. 39, no. 1, pp. 782–792, Mar. 2024.
- [30] L. Dalessandro, U. Drofenik, S. Round, and J. Kolar, "A novel hysteresis current control for three-phase three-level PWM rectifiers," in *Proc. Annu. IEEE Appl. Power Electron. Conf. Expo.*, vol. 1, 2005, pp. 501–507.
- [31] Z. Mao, X.-G. Yan, B. Jiang, and S. K. Spurgeon, "Sliding mode control of nonlinear systems with input distribution uncertainties," *IEEE Trans. Autom. Control*, vol. 68, no. 10, pp. 6208–6215, Oct. 2023.
- [32] M. Eissa, S. Leeb, G. Verghese, and A. Stankovic, "Fast controller for a unity-power-factor PWM rectifier," *IEEE Trans. Power Electron.*, vol. 11, no. 1, pp. 1–6, Jan. 1996.
- [33] P. Rodriguez, A. Luna, I. Candela, R. Mujal, R. Teodorescu, and F. Blaabjerg, "Multiresonant frequency-locked loop for grid synchronization of power converters under distorted grid conditions," *IEEE Trans. Ind. Electron.*, vol. 58, no. 1, pp. 127–138, Jan. 2011.
- [34] J. Matas, M. Castilla, J. Miret, L. García de Vicuña, and R. Guzman, "An adaptive prefiltering method to improve the speed/accuracy tradeoff of voltage sequence detection methods under adverse grid conditions," *IEEE Trans. Ind. Electron.*, vol. 61, no. 5, pp. 2139–2151, May 2014.
- [35] A. Isidori, *Nonlinear Control Systems*, 3rd ed., New York, USA: Springer-Verlag, April 2013.



Jose-Pascual Chico-Villegas (Student Member, IEEE) received the B.S. degree in mechanical engineering from the Technical University of Valencia, Valencia, Spain, 2018, and the M.S. degree in automatic systems and industrial electronics engineering in 2021 from the Technical University of Catalonia, Barcelona, Spain, where he is currently working toward the Ph.D. degree with the Department of Automatic Control.

His research interests include power electronics and nonlinear and predictive control.



Ramon Guzman (Senior Member, IEEE) received the B.S., M.S., and Ph.D. degrees in telecommunications engineering from the Technical University of Catalonia, Barcelona, Spain, in 1999, 2004, and 2016, respectively.

He is currently an Associate Professor with the Department of Automatic Control, Technical University of Catalonia. His research interests include nonlinear and adaptive control for three-phase power converters.

Dr. Guzman is a Member of the IEEE Industrial Electronics Society and becomes to the Renewable Energy Systems Subcommittee of Power Electronics Technical Committee of IES. He is an Associate Editor of the IEEE TRANSACTIONS ON INDUSTRIAL ELECTRONICS.



Luis Garcia de Vicuña received the M.S. and Ph.D. degrees in telecommunication engineering from the Technical University of Catalonia, Barcelona, Spain, in 1980 and 1990, respectively, and the Ph.D. degree in electrical engineering from Paul Sabatier University, Toulouse, France, in 1992.

From 1980 to 1982, he was an Engineer with a control applications company at Spain. He is currently a Full Professor with the Department of Electronic Engineering, Technical University of

Catalonia, where he teaches courses on power electronics. His research interests include power electronics modeling, simulation and control, active power filtering, and high-power-factor ac/dc conversion.



Miguel Castilla received the B.S., M.S., and Ph.D. degrees in telecommunication engineering from the Technical University of Catalonia, Barcelona, Spain, in 1988, 1995, and 1998, respectively.

Since 2019, he has been a Full Professor with the Department of Electronic Engineering, Technical University of Catalonia, where he teaches courses on control of power electronics converters. His research interests include power electronics, control, renewable energy systems, and electrical microgrids.



Àngel Borrell received the B.S. degree in electrical engineering, the M.S. degree in automation and industrial electronics engineering, and the Ph.D. degree in electronics engineering from the Technical University of Catalonia, Barcelona, Spain, in 1993, 2006, and 2012, respectively.

Since 1994, he has been an Associate Professor with the Department of Electrical Engineering, Escola Universitària Salesiana de Sarrià, Autonomous University of Barcelona, Barcelona, Spain, where he teaches courses on electrical machines and automation. His research interests include power electronics, electric motor drives, and renewable energy systems.